

Probing the distant universe with a very luminous fast radio burst at redshift 1

Stuart D. Ryder^{1,2}, Keith W. Bannister³, S. Bhandari^{4,5}, A. T. Deller⁶, R. D. Ekers^{3,7},
 Marcin Glowacki⁷, Alexa C. Gordon⁸, Kelly Gourdjji⁶, C. W. James⁷,
 Charles D. Kilpatrick⁸, Wenbin Lu⁹, Lachlan Marnoch^{1,2,3,10}, V. A. Moss³,
 J. Xavier Prochaska^{11,12,13}, Hao Qiu¹⁴, Elaine M. Sadler^{15,3}, Sunil Simha¹¹,
 Mawson W. Sammons⁷, Danica R. Scott⁷, Nicolas Tejos¹⁶, R. M. Shannon^{6,*}

¹School of Mathematical and Physical Sciences, Macquarie University, NSW 2109, Australia

²Astronomy, Astrophysics and Astrophotonics Research Centre, Macquarie University, Sydney, NSW 2109, Australia

³Australia Telescope National Facility, CSIRO, Space and Astronomy, PO Box 76, Epping, NSW 1710, Australia

⁴ASTRON, Netherlands Institute for Radio Astronomy, Oude Hoogeveensedijk 4, 7991 PD Dwingeloo, The Netherlands

⁵Joint institute for VLBI ERIC, Oude Hoogeveensedijk 4, 7991 PD Dwingeloo, The Netherlands

⁶Centre for Astrophysics and Supercomputing, Swinburne University of Technology, Hawthorn, VIC 3122, Australia

⁷International Centre for Radio Astronomy Research, Curtin Institute of Radio Astronomy,
 Curtin University, Perth, Western Australia, Australia.

⁸Center for Interdisciplinary Exploration and Research in Astrophysics (CIERA) and Department of Physics and Astronomy,
 Northwestern University, Evanston, IL 60208, USA

⁹Departments of Astronomy and Theoretical Astrophysics Center, UC Berkeley, Berkeley, CA 94720, USA

¹⁰ ARC Centre of Excellence for All-Sky Astrophysics in 3 Dimensions (ASTRO 3D), Australia

¹¹ Department of Astronomy and Astrophysics, University of California, Santa Cruz, CA 95064, USA

¹² Kavli Institute for the Physics and Mathematics of the Universe, 5-1-5 Kashiwanoha, Kashiwa, 277-8583, Japan

¹³Simons Pivot Fellow

¹⁴SKA Observatory, Jodrell Bank, Lower Withington, Macclesfield, SK11 9FT, UK

¹⁵Sydney Institute for Astronomy, School of Physics A28, University of Sydney, NSW 2006, Australia

¹⁶Instituto de Física, Pontificia Universidad Católica de Valparaíso, Casilla 4059, Valparaíso, Chile

*To whom correspondence should be addressed; E-mail: rshannon@swin.edu.au.

Fast radio bursts are millisecond-duration pulses of radio emission that have been found to originate at extragalactic distances. The bursts show dispersion imparted by intervening plasma, with the bulk attributed to the intergalactic medium. Here we report the discovery of a burst, FRB 20220610A, in a complex host galaxy system at a redshift of $z = 1.016 \pm 0.002$. The relationship between its redshift and dispersion confirm that the bulk of the baryonic matter was ionized and in the intergalactic medium when the universe was almost half its present age. The burst shows evidence for passage through a significant additional column of turbulent and magnetized high-redshift plasma. It extends the maximum observed burst energy by a factor of four, confirming the presence of an energetic burst population at high redshift.

Fast radio bursts (FRBs, (1, 2)) have emerged as an invaluable cosmological tool. Free electrons along the propagation path from the FRB source to the observer impart a frequency-dependent time delay (dispersion) on the impulsive radio signal. This dispersion provides a direct measure of the total free electron column (dispersion measure, DM) between the FRB source and observer. FRBs localized to host galaxies at different redshifts exhibit a positive correlation between total electron column and host redshift, referred to as the “Macquart relation” (3). Analysis of FRBs on this relation yields an independent measurement of the cosmic baryon fraction and the present-day expansion rate of the universe (4). To date, this relation has been demonstrated with securely identified host galaxies only to modest redshift ($z \lesssim 0.5$). Some unlocalized FRBs have DMs consistent with redshifts > 1 (5); conversely, a burst with large DM has been associated with a galaxy at moderate redshift in at least one case (6). Consequently, it is unclear whether high-DM FRBs commonly reside in relatively nearby hosts that impart a significant dispersion contribution of their own.

We have been searching for (7) and localizing (8) FRBs using the Australian Square Kilo-

metre Array Pathfinder (ASKAP, (9)), a radio interferometer in Western Australia comprising thirty-six 12-m antennas. Each antenna is equipped with phased-array receiving systems, enabling 36 beams to be digitally formed across the focal plane, covering approximately 30 square degrees. We search for FRBs in real-time in the incoherent sum of the intensities of each antenna in each beam. When an FRB is detected, voltage buffers are downloaded, correlated, calibrated, and imaged, enabling the position of the burst to be measured to an accuracy of typically a few tenths of an arcsecond (10, 11). FRB 20220610A was detected in a field containing a previously discovered burst (11), in observations centred at a frequency of 1271.5 MHz and a time resolution of 1.18 ms. FRB 20220610A is immediately notable for having a high DM of $1457.624 \pm 0.001 \text{ pc cm}^{-3}$; of the 54 bursts detected by ASKAP, only one (FRB 20210407E, (4)) has a higher DM (12). A dedispersed dynamic spectrum of the burst is shown in Figure 1, and properties of the burst are listed in Table 1.

When the burst was detected, voltage buffers were downloaded, enabling a sub-arcsecond localization. The 2 s dispersive sweep of the burst across the band and 2.4 s latency in the detection system resulted in only the lowest 88 MHz of the burst being captured in the 3.1 s duration voltage buffer. This nevertheless proved sufficient to localize the burst to a precision of 0.5 arcsec. We also used the voltage data to reconstruct the high time resolution and polarimetric properties of the burst. After correcting for dispersive smearing, the burst shows an exponentially decreasing tail consistent with scatter broadening due to turbulence in intervening plasma (13). The pulse broadening time is measured to be $0.511 \pm 0.012 \text{ ms}$ at a reference frequency of 1148 MHz assuming a ν^{-4} frequency dependence. We find strong evidence for Faraday rotation, with the rotation measure (RM) measured to be $215 \pm 2 \text{ rad m}^{-2}$. After correcting for Faraday rotation we observe the pulse to have a linear polarization fraction of greater than 96%. The high fractional linear polarization allows us to place a limit on Faraday dispersion (σ_{RM}) reported for other FRBs (14) and induced by fluctuations in rotation measure in

intervening turbulent plasma, constraining $\sigma_{\text{RM}} < 0.6 \text{ rad m}^{-2}$.

We undertook ground-based optical and infrared observations to identify and characterize the burst host galaxy (*11*). The images show an extended, multi-component morphology, where the burst position is coincident with one component (see Figure 2). Based on a Bayesian framework for assessing the chance of coincidence between transients and host galaxies (*15*), we find the probability of correct association to be greater than 99.99% and conclude the association is robust. Simultaneous optical and infrared spectroscopy of components A, B and C (Figure 2) with the Very Large Telescope (VLT) resulted in the detection of multiple emission lines, which yield (*11*) a redshift for the host system of 1.016 ± 0.002 . A complete summary of properties of the host can be found in Table 1. While the complex has a total stellar mass and star formation history comparable to that of nearby FRB hosts (*16, 17*), the morphology is markedly different. The total mass is measured to be approximately 10^{10} solar masses and we estimate the current star formation rate to be 0.4 solar masses per year (*11*).

The presence of two bright clumps A and C (separated by a distance of 16 kpc), and the diffuse feature B between them, is suggestive of two galaxies interacting or merging. It is also possible that the morphology is due to structure within a single galaxy, since at these redshifts as many as half of all galaxies show clumpy morphologies (*18*). However, this latter possibility is less likely, given the large spatial separation between the components. Additionally, component A appears brightest in the K_s -band image (most likely due to having an older stellar population), but is well displaced from the overall centroid of the optical light in g - and R -band, contrary to what is expected for a single undisturbed galaxy at this redshift. Higher spatial resolution should be able to discriminate between the components forming via gravitational instabilities in gas-rich disks (*19, 20*), or if an interaction or merger event is in progress (*21*).

The burst dispersion extends the Macquart relation to higher redshift. Figure 3 shows the relationship between dispersion measure and redshift for the ASKAP FRB sample. Subtracting

off a model for the Milky-Way contribution to the observed DM (11), we estimate an extragalactic DM of $\approx 1376 \text{ pc cm}^{-3}$, requiring a high column density of ionized gas between the FRB and Earth. This confirms the inference from other experiments (e.g. the Ly α forest; (22)) that the gas of the cosmic web is highly ionized. Furthermore, the detection of FRBs at $z > 1$ enables additional opportunities to study the nature of ionized plasma between, around, and within distant galaxies. For example, one expects a sightline to $z = 1$ to intersect several halos of galaxies comparable to our own (23). Follow-up observations will identify all such galaxies towards FRB 20220610A and permit studies of their circumgalactic medium (24). Last, the extension of the Macquart relation to $z \sim 1$ paves the way to yet higher redshifts and potential analysis of He II reionization.

We find significant excess DM of approximately 650 pc cm^{-3} relative to the median expectation from the Macquart relation — equivalent to 1300 pc cm^{-3} in the host rest frame (11). The scatter broadening and Faraday rotation of FRB 20220610A provide a unique opportunity to investigate the properties of plasma at high redshift. This observed dispersion excess could be due to any combination of gas in the immediate vicinity of the source, the interstellar medium of the host galaxy, or foreground intervening gas. The absence of strong Faraday rotation or depolarization contrasts to other FRB sources which show excess dispersion (6). This suggests the excess dispersion for FRB 20220610A originates in a less magnetoionically active plasma, such as in the interstellar medium of the host galaxy, rather than primarily in the circum-burst media hypothesized for other sources (11, 14, 25). Models imply that the DM of a typical spiral galaxy is unlikely to exceed a few hundred pc cm^{-3} except in extreme edge-on systems, but higher DM values can plausibly be produced by high-density clumps of gas within the host galaxy (26), particularly given that galaxies at $z \sim 1$ have a substantially higher fraction of their baryons in gas rather than stars. It is also possible that the dispersion originates from structure in the foreground intergalactic medium, or is the result of additional ionized material associated

with a putative galaxy merger.

The burst extends the maximum characteristic energy of FRBs and requires revision of models of the population. The bandwidth-averaged fluence for this event is 45 ± 5 Jy ms, implying an energy of $(6.4 \pm 0.7) \times 10^{32}$ erg Hz⁻¹ (11). This exceeds the characteristic E_{max} derived from previous FRB population models (4), suggesting FRBs to be even more extreme phenomena than previously thought. Using previous methods (27), we re-estimate the characteristic maximum FRB energy to be $E_{\text{max}} = 5_{-2}^{+3} \times 10^{32}$ erg Hz⁻¹. This rules out the lower range of allowed maximum FRB energies from previous estimates (4, 28, 29). The presence of further high-redshift high-luminosity bursts would challenge the model and further extend burst energetics.

The burst energy, $\sim 2 \times 10^{42}$ erg, is the highest in all unambiguously localized FRBs (Figure 3). Based on statistical analysis of the FRB rate function, this is near the maximum energy that the entire FRB source population can produce. This provides a stress test for the emission models of FRBs. In one class of models, the emission is produced near the surface of a neutron star. From the luminosity of the burst $\sim 3 \times 10^{46}$ erg s⁻¹ in the host-galaxy's rest frame, one infers an electric field strength of $1.4 \times 10^{12}(r/10 \text{ km})^{-1}$ electrostatic units, for a linearly polarized wave. This is a few percent of the Schwinger field strength for emission from near the neutron star surface ($r \sim 10$ km), and an electric field component of this strength parallel to the local magnetic field would be quickly shielded by copious pair production. This could cause a suppression of the FRB rate above this luminosity. In the other class of models, FRBs are produced by a shock driven by relativistic ejecta accompanied by a magnetar flare. In these models, the radiative efficiency is very low ($\lesssim 10^{-5}$) and hence the required ejecta energy would be $\gtrsim 10^{47}$ erg, while the total flare energy may be much higher. It is possible that FRB 20220610A is produced by one of the most energetic magnetic flares in the universe.

References

1. D. R. Lorimer, M. Bailes, M. A. McLaughlin, D. J. Narkevic, F. Crawford, *Science* **318**, 777 (2007).
2. E. Petroff, J. W. T. Hessels, D. R. Lorimer, *Astron. Astrophys. Rev.* **30**, 2 (2022).
3. J. P. Macquart, *et al.*, *Nature* **581**, 391 (2020).
4. C. W. James, *et al.*, *Mon. Not. R. Astro. Soc.* (2022).
5. S. Bhandari, *et al.*, *Mon. Not. R. Astro. Soc.* **475**, 1427 (2018).
6. C. H. Niu, *et al.*, *Nature* **606**, 873 (2022).
7. R. M. Shannon, *et al.*, *Nature* **562**, 386 (2018).
8. K. W. Bannister, *et al.*, *Science* **365**, 565 (2019).
9. A. W. Hotan, *et al.*, *Publ. Astron. Soc. Australia* **38**, e009 (2021).
10. C. K. Day, *et al.*, *Publ. Astron. Soc. Australia* **38**, e050 (2021).
11. Materials and methods are available as supplementary materials .
12. FRB20210407E was also found at low Galactic latitude ($b = 6.7^\circ$), suggesting a large Milky-Way contribution to the dispersion measure .
13. P. A. G. Scheuer, *Nature* **218**, 920 (1968).
14. Y. Feng, *et al.*, *Science* **375**, 1266 (2022).
15. K. Aggarwal, *et al.*, *Astrophys. J.* **911**, 95 (2021).
16. S. Bhandari, *et al.*, *Astrophys. J.* **901**, L20 (2020).

17. A. C. Gordon, *et al.* (in prep).
18. Y. Guo, *et al.*, *Astrophys. J.* **800**, 39 (2015).
19. D. M. Elmegreen, B. G. Elmegreen, S. Ravindranath, D. A. Coe, *Astrophys. J.* **658**, 763 (2007).
20. R. Genzel, *et al.*, *Astrophys. J.* **733**, 101 (2011).
21. B. Ribeiro, *et al.*, *Astron. & Astrophys.* **608**, A16 (2017).
22. T. S. Kim, *et al.*, *Mon. Not. R. Astro. Soc.* **501**, 5811 (2021).
23. J. X. Prochaska, Y. Zheng, *Mon. Not. R. Astro. Soc.* **485**, 648 (2019).
24. J. X. Prochaska, *et al.*, *Science* **366**, 231 (2019).
25. D. Michilli, *et al.*, *Nature* **553**, 182 (2018).
26. J. Xu, J. L. Han, *Research in Astronomy and Astrophysics* **15**, 1629 (2015).
27. C. W. James, *et al.*, *Mon. Not. R. Astro. Soc.* **509**, 4775 (2022).
28. R. Luo, *et al.*, *Mon. Not. R. Astro. Soc.* **494**, 665 (2020).
29. K. Shin, *et al.*, *arXiv e-prints* p. arXiv:2207.14316 (2022).
30. J. M. Cordes, T. J. W. Lazio, *arXiv e-prints* pp. astro-ph/0207156 (2002).
31. J.-P. Macquart, *et al.*, *Publ. Astron. Soc. Australia* **27**, 272 (2010).
32. R. M. Shannon, *Transient Name Server Fast Radio Bursts* **1403**, 1 (2022).
33. C. K. Day, *et al.*, *Mon. Not. R. Astro. Soc.* **497**, 3335 (2020).

34. A. T. Deller, *et al.*, *Pub. Astron. Soc. Pacific* **123**, 275 (2011).
35. THE CASA TEAM, *et al.*, *arXiv e-prints* p. arXiv:2210.02276 (2022).
36. C. K. Day, *et al.*, *Publ. Astron. Soc. Australia* **38**, e050 (2021).
37. J. J. Condon, *et al.*, *Astron. J.* **115**, 1693 (1998).
38. C. L. Hale, *et al.*, *Publ. Astron. Soc. Australia* **38**, e058 (2021).
39. H. Cho, *et al.*, *Astrophys. J.* **891**, L38 (2020).
40. H. Qiu, *et al.*, *Monthly Notices of the Royal Astronomical Society* **497**, 1382 (2020).
41. G. Ashton, *et al.*, *The Astrophysical Journal Supplement Series* **241**, 27 (2019). Publisher: American Astronomical Society.
42. J. E. Everett, J. M. Weisberg, *Astrophys. J.* **553**, 341 (2001).
43. A. Drlica-Wagner, *et al.*, *arXiv* p. arXiv:2203.16565 (2022).
44. W.-f. Fong, *et al.*, *arXiv e-prints* p. arXiv:2206.01763 (2022).
45. A. U. Landolt, *Astron. J.* **104**, 340 (1992).
46. M. Kissler-Patig, *et al.*, *Astron. & Astrophys.* **491**, 941 (2008).
47. W. Freudling, *et al.*, *Astron. & Astrophys.* **559**, A96 (2013).
48. M. F. Skrutskie, *et al.*, *The Astronomical Journal* **131**, 1163 (2006).
49. K. Barbary, *Astrophysics Source Code Library, record ascl:1811.004* p. ascl:1811.004 (2018).
50. K. Barbary, *Journal of Open Source Software* **1**, 58 (2016).

51. J. Vernet, *et al.*, *Astron. & Astrophys.* **536**, A105 (2011).
52. J. Prochaska, *et al.*, *The Journal of Open Source Software* **5**, 2308 (2020).
53. K. Glazebrook, J. A. Peacock, L. Miller, C. A. Collins, *Mon. Not. R. Astro. Soc.* **275**, 169 (1995).
54. C. De Breuck, *et al.*, *Astron. J.* **123**, 637 (2002).
55. M. Kajisawa, *et al.*, *Publ. Astron. Soc. J.* **52**, 61 (2000).
56. C. Leitherer, *et al.*, *Astrophys. J.* **123**, 3 (1999).
57. B. D. Johnson, J. Leja, C. Conroy, J. S. Speagle, *Astrophys. J.* **254**, 22 (2021).
58. C. Conroy, J. E. Gunn, M. White, *Astrophys. J.* **699**, 486 (2009).
59. C. Conroy, J. E. Gunn, *Astrophys. J.* **712**, 833 (2010).
60. J. S. Speagle, *Mon. Not. R. Astro. Soc.* **493**, 3132 (2020).
61. G. Chabrier, *Pub. Astron. Soc. Pacific* **115**, 763 (2003).
62. J. A. Cardelli, G. C. Clayton, J. S. Mathis, *Astrophys. J.* **345**, 245 (1989).
63. A. Gallazzi, S. Charlot, J. Brinchmann, S. D. M. White, C. A. Tremonti, *Mon. Not. R. Astro. Soc.* **362**, 41 (2005).
64. J. Leja, A. C. Carnall, B. D. Johnson, C. Conroy, J. S. Speagle, *Astrophys. J.* **876**, 3 (2019).
65. M. Bhardwaj, *et al.*, *Astrophys. J.* **910**, L18 (2021).
66. S. Inoue, *Mon. Not. R. Astro. Soc.* **348**, 999 (2004).

67. J. X. Prochaska, S. Simha, C. Law, N. Tejos, M. Neeleman, Frb, <https://zenodo.org/record/3403651#.YRxkcBMzZKA> (2019).
68. Planck Collaboration, *et al.*, *Astron. & Astrophys.* **641**, A6 (2020).
69. C. W. James, *et al.*, *Publ. Astron. Soc. Australia* **36**, e009 (2019).
70. P. Kumar, *et al.*, *Mon. Not. R. Astro. Soc.* **500**, 2525 (2021).
71. J. P. Macquart, *et al.*, *Astrophys. J.* **872**, L19 (2019).
72. C. W. James, *et al.*, *Mon. Not. R. Astro. Soc.* **510**, L18 (2022).
73. C. W. James, J. X. Prochaska, E. M. Ghosh, zdm, <https://zenodo.org/record/5213780#.YRxxh5BMzZKA> (2021).
74. B. J. Burn, *Mon. Not. R. Astro. Soc.* **133**, 67 (1966).
75. R. Anna-Thomas, *et al.*, *arXiv e-prints* p. arXiv:2202.11112 (2022).
76. N. D. R. Bhat, J. M. Cordes, F. Camilo, D. J. Nice, D. R. Lorimer, *Astrophys. J.* **605**, 759 (2004).
77. R. N. Manchester, G. B. Hobbs, A. Teoh, M. Hobbs, *Astron. J.* **129**, 1993 (2005).
78. R. M. Shannon, S. Johnston, *Mon. Not. R. Astro. Soc.* **435**, L29 (2013).
79. K.-G. Lee, *et al.*, *Astrophys. J.* **928**, 9 (2022).

Acknowledgments

We thank K. Heintz for contributions to the FURBY project, and N. Förster-Schreiber and K. Glazebrook for discussions. We thank ATNF staff for supporting CRAFT observations with

ASKAP. Based on observations collected at the European Southern Observatory under ESO programmes 0105.A-0687 and 1108.A-0027. The Australian SKA Pathfinder is part of the Australia Telescope National Facility (<https://ror.org/05qajvd42>) which is managed by CSIRO. Operation of ASKAP is funded by the Australian Government with support from the National Collaborative Research Infrastructure Strategy. ASKAP uses the resources of the Pawsey Supercomputing Centre. Establishment of ASKAP, the Murchison Radio-astronomy Observatory (MRO) and the Pawsey Supercomputing Centre are initiatives of the Australian Government, with support from the Government of Western Australia and the Science and Industry Endowment Fund. Some of the data presented herein were obtained at the W. M. Keck Observatory, which is operated as a scientific partnership among the California Institute of Technology, the University of California, and the National Aeronautics and Space Administration. The Observatory was made possible by the generous financial support of the W. M. Keck Foundation. We acknowledge the Wajarri Yamatji people as the traditional owners of the MRO site. We recognize and acknowledge the very significant cultural role and reverence that the summit of Maunakea has always had within the indigenous Hawaiian community. We are most fortunate to have the opportunity to conduct observations from this mountain. SB is supported by a Dutch Research Council (NWO) Veni Fellowship (VI.Veni.212.058). ATD and KG acknowledge support through ARC Discovery Project DP200102243. ATD and RMS acknowledge support through Australian Research Council Discovery (ARC) Project DP220102305. CWJ and MG acknowledge support through ARC DP DP210102103. RMS acknowledges support through ARC Future Fellowship FT190100155. JXP, SS, CK, ACG, and NT, as members of the Fast and Fortunate for FRB Follow-up team, acknowledge support from National Science Foundation grants AST-1911140, AST-1910471 and AST-2206490.

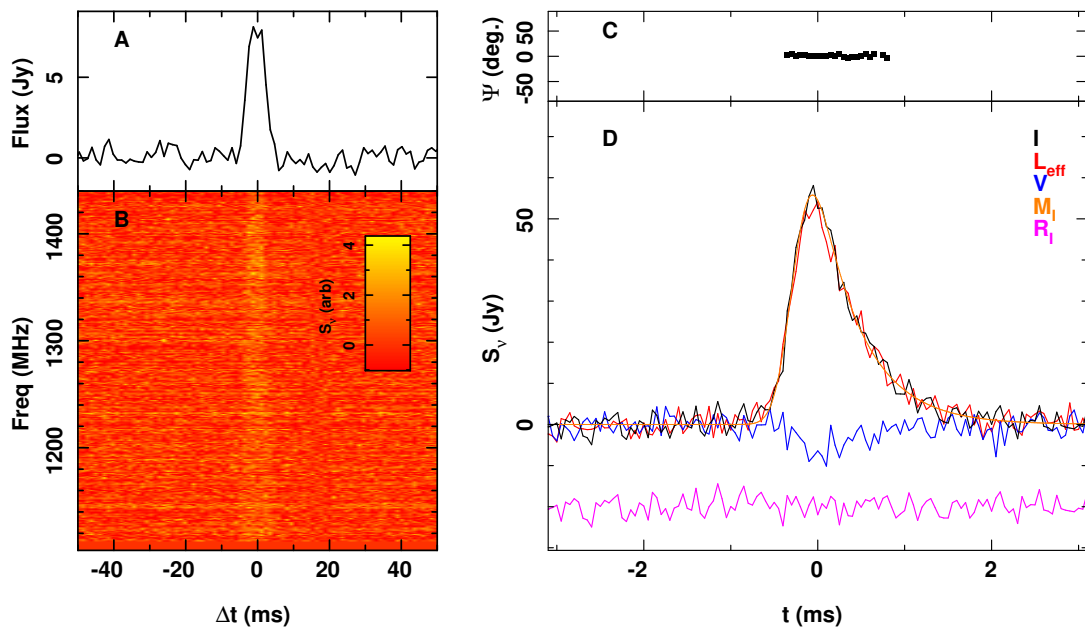


Figure 1. FRB 20220610A. Left: FRB as observed in the incoherently summed data stream. The pulse width is dominated by intra-channel dispersion smearing. Panel A shows the integrated pulse profile, while panel B shows the dedispersed burst dynamic spectrum, highlighting an unmodulated spectrum unlike many lower DM ASKAP FRBs (7). Right: High time resolution data produced from the downloaded voltages. Panel C shows linear polarization position angle Ψ , while panel D shows the integrated pulse profile. We show total intensity I , linear polarization L_{eff} (II), Stokes V , and the maximum likelihood model for Stokes I is labelled M_I . We show the residuals R_I between I and M_I offset from zero by -20 Jy.

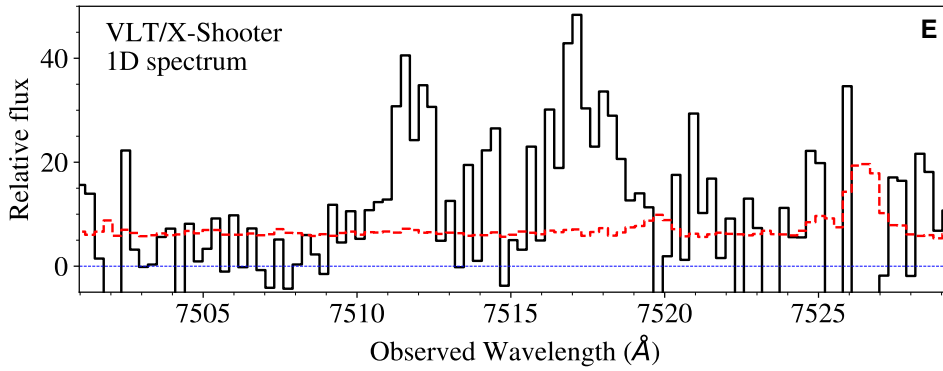
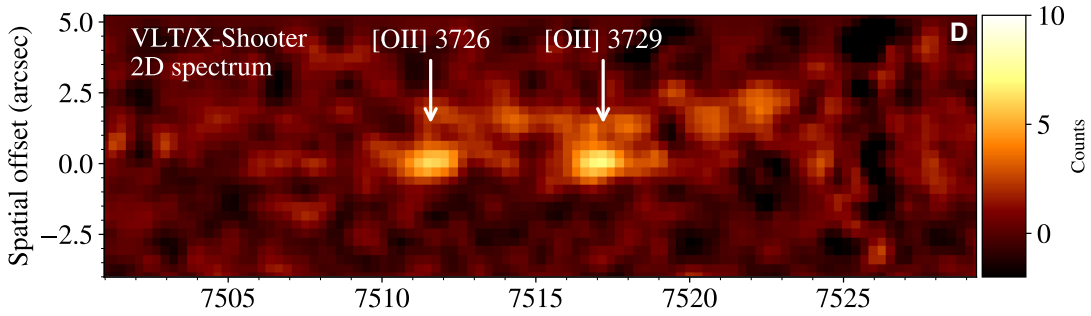
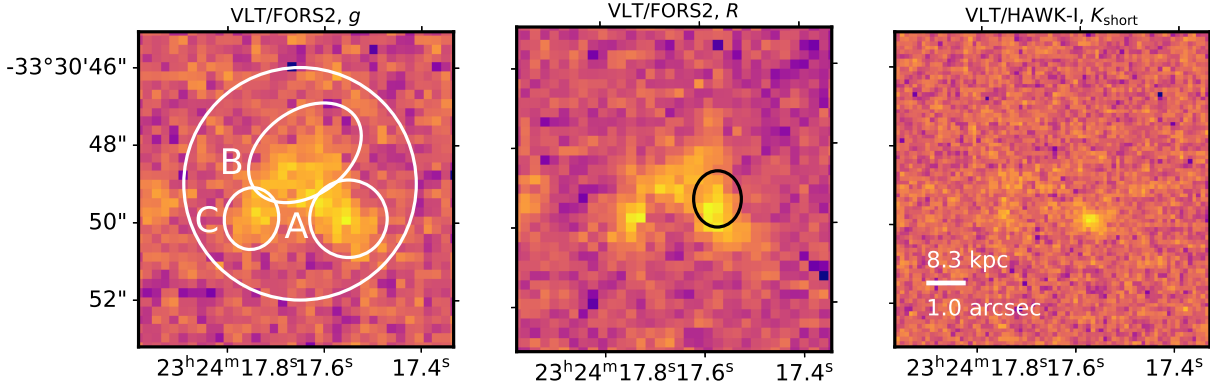


Figure 2. Optical and infrared observations of the FRB 20220610A host. A: g -band image, with the ellipses outlining the apertures used for each clump. The unlabeled circle is the aperture used for the entire combined object. B: R -band image, with the FRB localization and uncertainty (68% confidence) indicated by the black ellipse. C: K_s band image. The scale bar shows the angular scale and corresponding projected physical scale at the host redshift. All three images are on the same scale. D: VLT/X-shooter detection of [O II] lines with rest wavelengths of 3726

and 3729 \AA from the host galaxy of FRB 20220610A at a slit position angle on the sky of 45° covering apertures A and B above. E: A 1D spectrum (black solid line) and its uncertainty (red dashed line) extracted from the 2D image with an aperture width of $1.8''$ full width at half maximum.

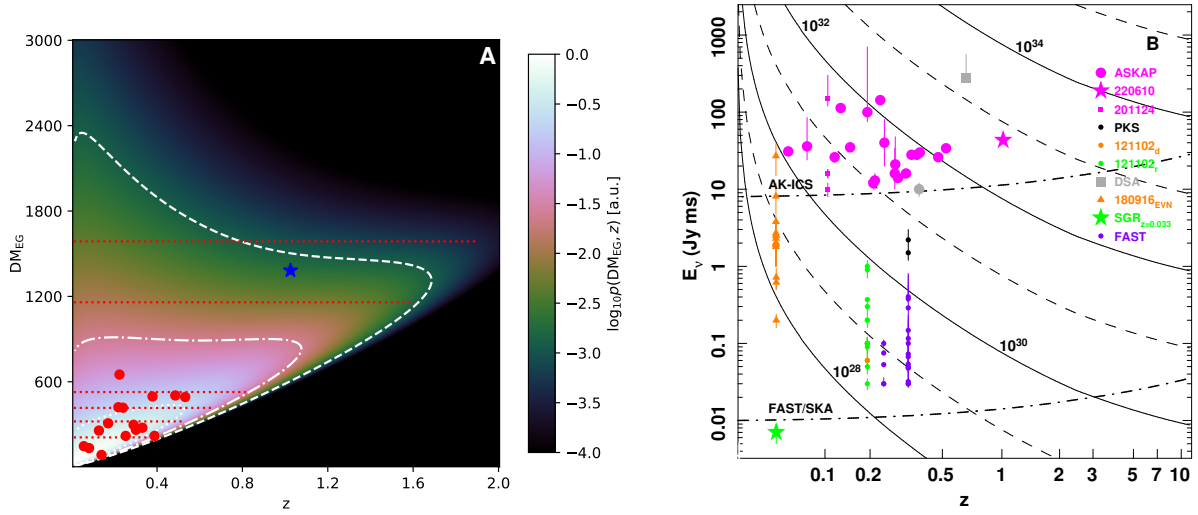


Figure 3. *Left:* Fast radio burst z - DM_{EG} distribution for the ASKAP incoherent sum (ICS) survey. Shown are localized FRBs (red circles showing host galaxy redshifts) and un-localized FRBs (red dotted lines showing 99% confidence interval for redshift). The color scale is proportional to the detection likelihood per dz and extragalactic dDM_{EG} increment (4) with an increased maximum energy $\log_{10} E_{\nu} [\text{erg Hz}^{-1}] = 32.7 \pm 0.2$ found in this work. Dotted, dash-dot, and dashed white contours contain 50%, 90%, and 99% of the probability mass. FRB 20220610A is shown with the blue star. *Right:* The fluence-redshift-luminosity properties of localized FRBs. FRB localisation instruments are noted in the top right. The magenta star is FRB 20220610A. The curved solid and dashed contours show energy density in units of erg Hz^{-1} . The dash-dotted lines show the sensitivity of our detection system (AK-ICS) and the more sensitive FAST and SKA telescopes. Repeating FRBs are shown at multiple fluences.

Table 1. Properties of FRB 20220610A and its host galaxy. The fluence is derived from filter-bank data recorded by the FRB detection system, which includes the full ASKAP bandwidth. The Milky-Way disk DM component is estimated from the NE2001 model (30).

Measured burst properties	
Dispersion Measure (DM)	$1457.624 \pm 0.001 \text{ pc cm}^{-3}$
Arrival time at 1271.5 MHz	2022-06-10 22:26:43.402
Fluence	$45 \pm 5 \text{ Jy ms}$
Right Ascension (J2000)	$23^{\text{h}}24^{\text{m}}17.569^{\text{s}} \pm 0.040^{\text{s}}$
Declination (J2000)	$-33^{\circ}30'49.37'' \pm 0.50''$
Galactic Longitude	8.8°
Galactic Latitude	-70.2°
Incoherent Detection S/N (1104 – 1440 MHz)	29.8
Image S/N (1104-1152 MHz)	81
Rotation Measure	$215 \pm 2 \text{ rad m}^{-2}$
Host galaxy properties	
Redshift	1.016 ± 0.002
Mass-weighted age (Gyr)	$1.02^{+1.64}_{-0.62}$
log(Total mass) (M_{\odot})	$10.11^{+0.18}_{-0.07}$
log(Stellar mass) (M_{\odot})	$9.98^{+0.14}_{-0.07}$
100 Myr SFR (M_{\odot}/yr)	0.40
log(Metallicity) (Z/Z_{\odot})	$-0.11^{+0.17}_{-1.68}$
g (mag)	24.15 ± 0.07
V (mag)	23.89 ± 0.13
R (mag)	23.78 ± 0.06
I (mag)	22.17 ± 0.07
z (mag)	21.95 ± 0.12
J (mag)	21.97 ± 0.07
K_s (mag)	22.08 ± 0.12
Inferred burst properties	
Intrinsic width (FWHM)	$0.41 \pm 0.01 \text{ ms}$
Implied FRB isotropic energy density	$6 \times 10^{32} \text{ erg Hz}^{-1}$
Milky-way disk DM contribution	31 pc cm^{-3}

Supplementary materials for Probing the distant universe with a very luminous fast radio burst at redshift 1

Authors: Stuart D. Ryder, Keith W. Bannister, S. Bhandari, A. T. Deller, R. D. Ekers, Marcin Glowacki, Alexa C. Gordon, Kelly Gourdji, C. W. James, Charles D. Kilpatrick, Wenbin Lu, Lachlan Marnoch, V. A. Moss, J. Xavier Prochaska, Hao Qiu, Elaine M. Sadler, Sunil Simha, Mawson W. Sammons, Danica R. Scott, Nicolas Tejos, & R. M. Shannon.

This PDF file includes

Materials and Methods

Supplementary Text

Figures S1 to S8

Tables S1 to S2

References 31-79

S1 Materials and Methods

S1.1 FRB detection

FRB 20220610A was detected as part of the Commensal Real-time ASKAP Fast Transient survey science project (31), which uses the Australian Square Kilometre Array Pathfinder (ASKAP (9)) to search for dispersed radio transients such as FRBs. ASKAP is an interferometer comprising 36 antennas, each of 12-m diameter. Each antenna is equipped with a phased array feed (PAF) receiver. The PAF receivers enable 36 beams to be digitally synthesized across the focal plane of the antenna, generating a total field-of-view of approximately 30 deg².

The current FRB detection system on ASKAP searches intensity data, incoherently summed across telescopes, in real time. Due to constraints on performance of the search system, only a subset of the 36 antennas are included in the real-time sum, with trade offs existing between the number of antennas included and the time resolution of the data searched. In the case of FRB 20220610A, the searches were conducted using 22 of the antennas, with a time resolution of 1.182 ms. In all cases a total bandwidth of 336 MHz is searched with a spectral resolution of 1 MHz. The search data streams are recorded to disk in pulsar filterbank¹ format for subsequent analysis in the case a burst is detected. Additional details of the search system have previously been provided along with earlier ASKAP FRB discoveries (8).

FRB searches with ASKAP are intended to be commensal with other observations. However, some observations are also conducted in *filler* mode. These observations occur during times where standard observations are not scheduleable. The observations were conducted at a central frequency of 1271.5 MHz with the configurable beam configuration in a hexagonal close pack configuration beam centers separated by 0.9 degree. FRB 20220610A was detected during filler observations, pointed towards FRB 220501C, an FRB previously detected by ASKAP (32).

¹<http://sigproc.sourceforge.net>

The burst was detected with a reported signal to noise ratio (S/N) of 29.8 in primary beam. As the ASKAP beams oversample the focal plane, the burst was detected with $S/N > 5$ in four adjacent beams. The burst width, at full width half maximum, as measured in the filterbank was 5.6 ± 0.4 ms. This is consistent with the 6.0 ms burst width expected from intrachannel dispersion smearing.

S1.2 FRB localization

The localisation of FRB 20220610A made use of the 3.1 s of saved voltage data from each ASKAP antenna triggered by the real-time detection described above. Due to the dispersive sweep of 2.04 s across the 336 MHz-wide ASKAP band, combined with the 2.4 s latency of the detection system, much of the FRB had already been lost from the voltage buffer before it was frozen and downloaded. Below a frequency of 1192 MHz, the FRB signal remained present in the saved data. Approximately 2.5 h after the FRB detection, a voltage download was triggered while observing the bright source PKS 0407-658, to be used for calibration purposes, followed shortly after by a voltage download on the Vela pulsar (used as a polarization calibrator).

The localisation of FRB 20220610A made use of the ASKAP FRB astrometric pipeline first described by (8), as extended by (33). Following the procedure laid out in these works, we correlated a small time window matching the dispersed FRB itself (forming the “gated” dataset), as well as the full 3.1s time window from the FRB voltage download (the “field” dataset) and the voltages downloaded while observing PKS 0407-658 (the “calibrator” dataset). Finally, the voltages downloaded while observing the Vela pulsar were also correlated (the “polcal” dataset).

The downloaded voltage data was processed using the “CELEBI” pipeline, which is based on the procedures detailed in (8) and (33) and will be fully described in a forthcoming publication (Scott et al., in prep). Voltage data was correlated using the DiFX software correlator (34), producing the four visibility datasets described above.

Calibration was derived from the calibrator dataset and applied to the gated, field, and polcal datasets as described by (33). After calibration, each dataset was imaged using CASA (35). Portions of the spectrum affected by radio frequency interference (for the field and polcal datasets) and the lack of FRB emission due to the limited voltage buffer size and FRB dispersion (for the target dataset) were flagged prior to imaging. Positions and corresponding uncertainties were measured in the image plane using the AIPS task JMFIT.

The target position was measured from the FRB image to be $23^{\text{h}}24^{\text{m}}17.559^{\text{s}} \pm 0.006^{\text{s}}$ $-33^{\circ}30'49.87'' \pm 0.07''$. Following the procedure detailed in (36), we used an ensemble of 7 background radio-continuum sources from our 3.1 second field image to estimate any systematic shift in the FRB position. These 7 sources were all the detections from this field image that were unresolved in the NRAO VLA Sky Survey (NVSS) (37). All sources were also present in the Rapid ASKAP Calibrator Survey (RACS) catalog (38). Neither catalogue is, however, ideal as a point of comparison; RACS is at lower frequency than our observations (and the initial data release is affected by astrometric errors of up to $\lesssim 1$ arcsecond) while NVSS is at higher frequency and lower angular resolution. We measure a small astrometric correction that is consistent at the 1σ level from each catalogue: $-0.16'' \pm 0.5''$ and $0.85'' \pm 0.5''$ in right ascension and declination respectively based on RACS catalogue positions, and $0.39'' \pm 0.5''$ and $0.14'' \pm 0.5''$ in right ascension and declination respectively based on NVSS catalogue positions. As we have no prior information to prefer one catalogue over the other, we take an unweighted average of the two offsets as our final correction: $0.12''$ and $0.50''$ in right ascension and declination respectively, while conservatively maintaining the uncertainty on the correction at $0.5''$ in each coordinate. This is equivalent to using an unweighted average of the RACS and NVSS reference positions for each source when performing the comparison to the field image positions, without reducing the corresponding reference position uncertainty. We note that should a more suitable reference catalogue be available (e.g., an astrometrically robust RACS-

mid catalogue at frequencies matching observations) the uncertainty on our systematic position correction would shrink by a factor of almost three; currently, it completely dominates the final position uncertainty. After applying this astrometric correction, the final FRB position is $23^{\text{h}}24^{\text{m}}17.569^{\text{s}} \pm 0.040^{\text{s}} -33^{\circ}30'49.37'' \pm 0.50''$.

S1.3 Beamforming and spectral-temporal polarimetry

The voltage data was also used to reconstruct a complex-valued time series of the electric field in two linear polarizations, and hence the I, Q, U, V Stokes parameters and measurements of the polarization properties of FRB 20220610A at a time resolution of 3 ns. The beamforming process used to achieve this has been previously outlined in (39) and is now incorporated into the CELEBI pipeline (Scott et al., in prep) already referred to above. In this pipeline, we apply per-antenna time delays to account for the difference in signal arrival times and apply a polyphase filterbank (PFB) inversion to obtain a single complex fine spectrum for each polarization per antenna. Calibration solutions were then applied, before spectra were summed across all antennas and deripped. Differential gain and phase between the two linearly polarized feeds was derived using the “polcal” dataset of the Vela pulsar (PSR J0835–4510). The FRB data was then coherently dedispersed (using the S/N-maximising $\text{DM} = 1457.624 \pm 0.001 \text{ pc cm}^{-3}$) and a Fourier transform inversion applied. Finally, the Stokes products are detected and the data averaged in time and frequency to the desired resolution.

S1.4 Burst scatter broadening

Determining the scattering time requires modelling the intrinsic burst profile. We model the intrinsic pulse as a Gaussian with a full width half maximum, w and amplitude a . The intrinsic pulse is then convolved with an exponential scattering kernel characterized by scattering time τ . We initially assume no frequency evolution due to the narrow fractional bandwidth of the

	FRB 20220610A	20190520B (6)
τ (ms)	0.511 ± 0.012	10 ± 2
ν_τ (GHz)	1.149	1.25
z	1.016 ± 0.002	0.241 ± 0.001
$\tau'_{1.4\text{GHz}}$ (ms)	1.88 ± 0.02	12 ± 2

Table S1: Observed scattering properties of FRBs observed with large excess DM, including FRB 20190520B and (6). We scale scattering timescale τ to 1.4 GHz in the host galaxy rest frame, assuming $\tau \propto \nu^{-4}$, to give $\tau'_{1.4\text{GHz}}$.

pulse. This model is fit to the temporal profile of the burst integrated over 88 MHz centred at 1149 MHz where the burst is present, and hence our effective reference frequency for the scattering time τ is 1149 MHz. Each 1 MHz channel is normalized to mean zero and standard deviation one to remove any radio frequency interference prior to summation in frequency.

We use a nested sampling approach (40), which implements the BILBY (41) PYTHON library to determine the best model. Assuming uniform priors on τ and w , the peak posterior parameters are $\tau = 0.511 \pm 0.012$ ms and $w = 0.407 \pm 0.012$ ms, as shown in Figure S1. The best fit model is plotted in Figure 1. Fitting to four 22 MHz sub-bands and assuming a $\tau \propto \nu^{-4}$ scaling yields a consistent result for the scattering time. We do not attempt to model the frequency behavior of the burst in detail owing to the small bandwidth captured in voltage data.

Taking the measured redshift of 1.016 along with our reference frequency of 1.149 GHz, and assuming a scattering index of $\tau \propto \nu^{-4}$, we scale to the host galaxy rest frame (indicated by \prime) to find $\tau'_{1.4\text{GHz}} = 1.88 \pm 0.02$ ms, and $w' = 0.202 \pm 0.006$ ms. To compare with other FRBs with large excess DMs above the Macquart relation, we also scale their observed scattering properties using the same method, as given in Table S1.

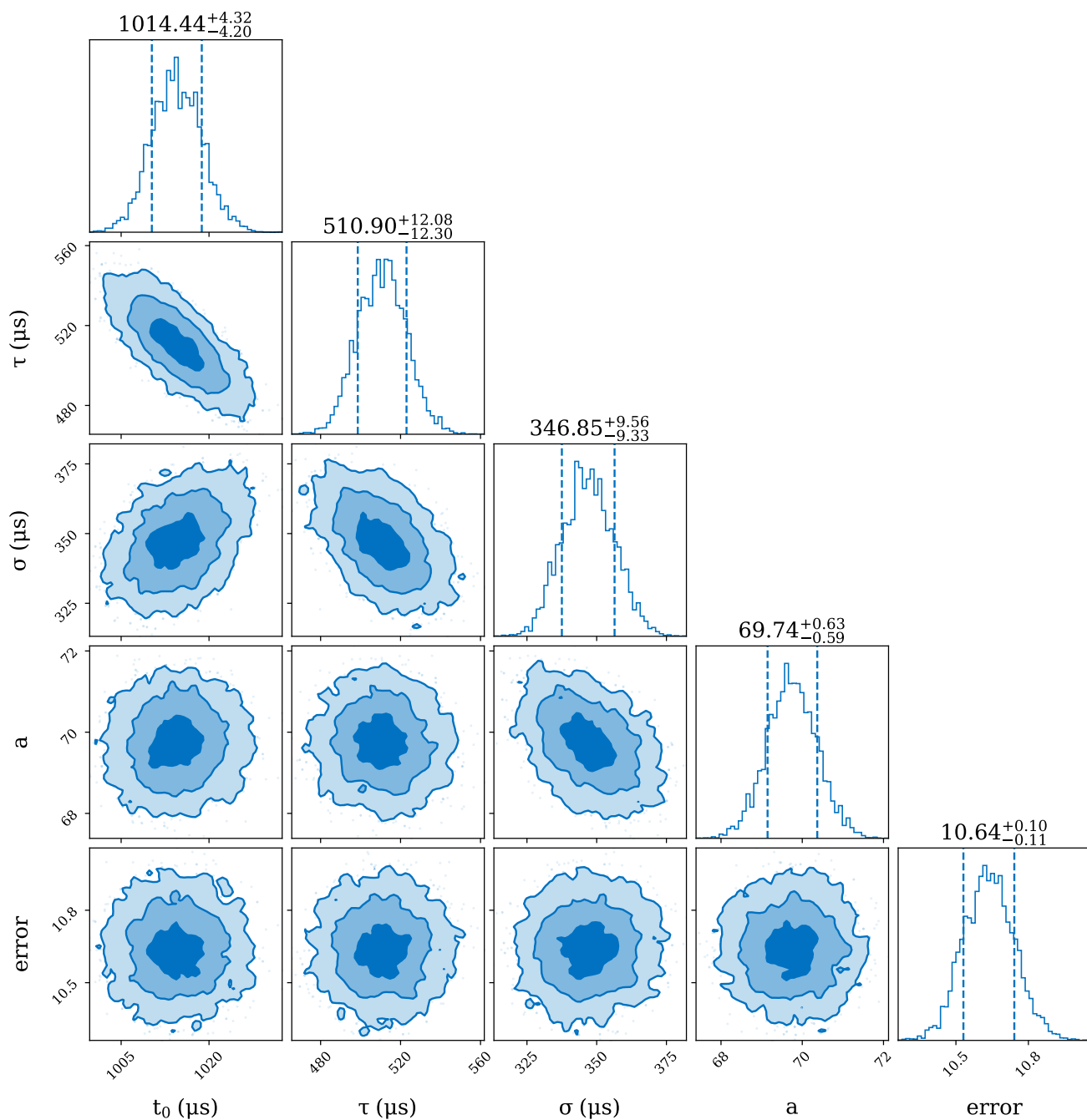


Figure S1: Posterior probabilities for the scattered gaussian model. Shaded regions contain 0.39, 0.86 and 0.99 the total probability mass. Results are listed in μs , except for a and $error$ parameters which have arbitrary scale, where $error$ is the standard deviation of the residuals to the fit. The full width at half maximum (FWHM), w , corresponds to $2\sqrt{2 \ln 2}\sigma$.

S1.5 Burst rotation measure

After polarimetric calibration, it was obvious that FRB 20220610A was highly linearly polarized, and that the Stokes Q and U parameters showed frequency dependent variation that we attribute to Faraday rotation in cold plasma.

As the polarization of the burst is constant in time, it is simplest to determine the rotation measure (RM) of the burst using a one-dimensional spectrum. We formed the spectrum by integrating over a 1.9 ms gate around the peak of the pulse. We used a Bayesian methodology previously applied to ASKAP detected FRBs (8). Briefly, we fitted for the expected frequency dependent variations in Stokes Q and U , while marginalizing over potential intensity variations in individual channels, finding a best-fit rotation measure of 215 rad m^{-2} . The pulse-averaged spectrum of the burst and the best fit model for the rotation measure induced change in the polarization position angle Ψ are presented in Figure S2.

The burst shows strong linear polarization with no evidence for polarization position angle changing across the pulse. If plotted on a Poincare sphere, the polarization vector would be constant and lie in the $Q - U$ plane. In Figure 1, we show the linear polarization projected onto this point. The noise statistics of this quantity are Gaussian, unlike the more general estimate of linear polarization $L = \sqrt{Q^2 + U^2}$ (33, 42).

S1.6 Optical and infrared imaging

Imaging of the location of FRB 20220610A was initially undertaken using the FOcal Reducer and low dispersion Spectrograph 2 (FORS2) on UT1 of the European Southern Observatory's Very Large Telescope (VLT) on Cerro Paranal. On-chip binning of 2×2 yielded a pixel scale of $0.25''$ over the $6.8' \times 6.8'$ field of view. Five exposures of 400 sec in the R_SPECIAL filter, with offsets of $\pm 10''$ between each, were obtained on 2022 July 1 UT, while a total of 10 exposures of 600 sec in the g filter were obtained across 2022 Oct 2-4 UT, in seeing of $0.9\text{--}1.0''$. The FORS2

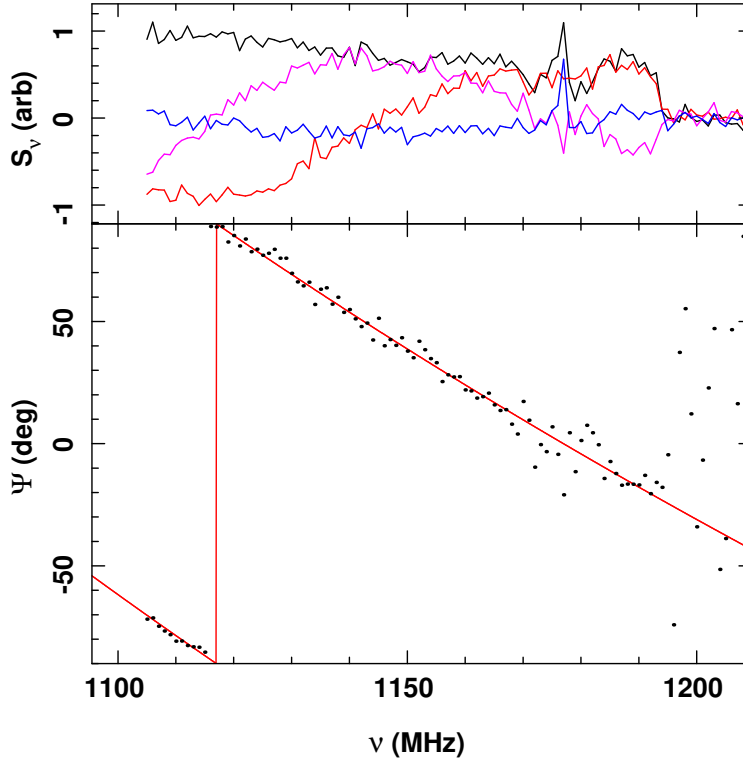


Figure S2: Pulse averaged spectrum of FRB 220610. *Top*: Spectra for Total Intensity (black), Stokes Q (red), Stokes U (magenta), and Stokes V (blue). The variation in flux density between Q and U is the result of Faraday rotation. The absence of FRB emission above ~ 1195 MHz is due to the highly dispersed FRB not being captured in the buffered voltages above this frequency. *Bottom*: Linear polarization position angle Ψ (black points). The maximum-likelihood model is shown as the red line.

images were processed in the same manner as described in (3), with the photometry calibrated against DELVE (43) for the g -band images and using the ESO FORS2 QC1² database for R -band.

Supplemental imaging of the host of FRB 20220610A was obtained with the Deep Imaging Multi-Object Spectrograph (DEIMOS) on the Keck-II 10m telescope on Maunakea, Hawaii on 2022 September 24 UT in the V , I , and z filters for 3×350 s in each. Atmospheric conditions

²http://archive.eso.org/bin/qc1.cgi?action=qc1_browse_table&table=fors2_photometry

Clump:	A	B	C
g	25.36 ± 0.07	25.13 ± 0.07	26.01 ± 0.09
R	24.98 ± 0.06	25.69 ± 0.08	24.82 ± 0.06
J	23.07 ± 0.08	23.84 ± 0.12	23.40 ± 0.13
K_s	22.92 ± 0.09	23.76 ± 0.15	> 23.66
$(R - K_s)$	2.06 ± 0.15	1.93 ± 0.23	< 1.16

Table S2: Photometric measurements for each of the clumps in the host of FRB 20220610A as marked on Figure 2.

were near-photometric with an average seeing of $0.9''$ and the field was observed at an average airmass of 1.7. All imaging was reduced following standard procedures in the `python`-based package `POTPYRI` see e.g., (44). Zero points for the stacked frames were derived using Landolt photometric standards (45) transformed into the DEIMOS photometric bands.

Near-infrared imaging was carried out with the HAWK-I camera (46) in combination with the GRAAL ground-layer adaptive optics system on UT4 of the VLT, covering a $7.5' \times 7.5'$ field at $0.106''/\text{pixel}$. Observations in the K_s filter were taken on 2022 July 24 UT, and in the J filter on 2022 September 29 UT in clear conditions and delivered image quality of $0.4\text{--}0.5''$. For each filter 15 integrations of 10 sec were averaged at each of 16 random offset positions within a $20''$ box. Image mosaics were processed using ESOReflex (47), with photometric calibration undertaken using the 2MASS point source catalogue (48).

For the DEIMOS imaging, aperture photometry was performed using a $3''$ host radius and a $4''$ to $7.5''$ background annulus (Table 1). For the VLT imaging two approaches were used to measure photometry: first, a single circular aperture with a radius of $3''$ encompassing the entire source (Table); and second, three ellipses defined by eye (as shown in **Figure 2a**) from the R -band imaging, to individually measure clumps A, B and C (Table S2). Both approaches, including background subtraction, were undertaken using the SEP package (49, 50).

S1.7 Optical and infrared spectroscopy

Spectroscopy covering the entire ultraviolet through near-infrared wavelength range of 0.3–2.48 μm was conducted with the X-shooter spectrograph (51) on UT3 of the VLT. Slit widths of 1.0", 0.9", and 0.9" yielded spectral resolutions of 5400, 8900, and 5600 in the UVB, VIS, and NIR arms, respectively, with 2×2 on-chip binning employed in the UVB and VIS detectors due to the faintness of the target.

Observations of the target were made at 2 slit position angles: the first on 2022 July 29 UT at a position angle of 45° covering clumps A and B shown in Fig. 2; and the second on 2022-September 23/24 UT at a position angle of 90° covering clumps A and C. At each position angle, a total of between 7200 and 7548 sec of integration time was accumulated in clear conditions and seeing 0.5–1.2", with frequent nodding of the target by $\pm 2.5''$ along the slit to assist with sky subtraction. Observations of the B9 V stars HD 138940 and HD 168852 were obtained to enable removal of telluric features, and of the spectrophotometric standard stars EG 21 and LTT 987 to allow relative flux calibration. The spectra were reduced with the PYPEIT data reduction pipeline (52) using standard techniques for image processing and wavelength calibration. The VIS science exposures were individually processed and the sky-subtracted 2D spectral images were co-added to maximize S/N.

From the spectroscopy of components A, B and C we were able to identify lines at 7510 and 7515 \AA associated with the [O II] 3726 and 3729 \AA forbidden transitions of ionized oxygen (Figure 2), and at 13228 \AA associated with the 6563 \AA $\text{H}\alpha$ transition. Together these lines confirm the redshift of the host to be 1.016 ± 0.002 .

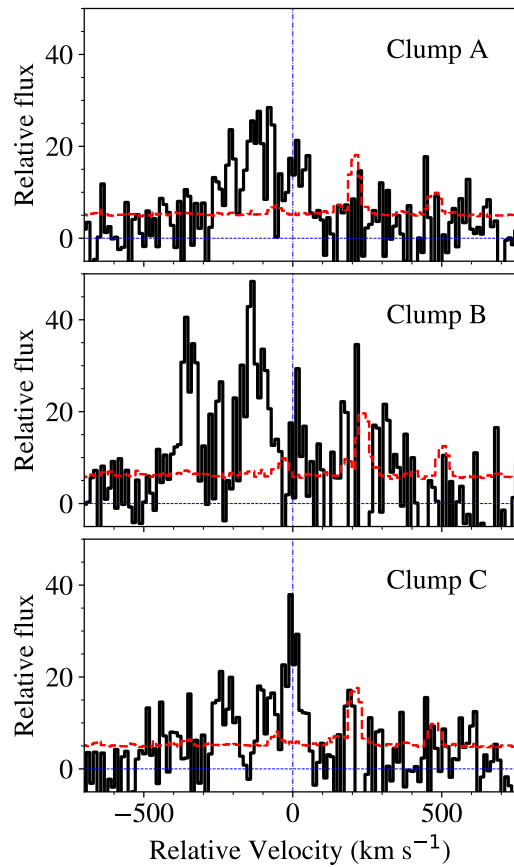


Figure S3: VLT/X-shooter spectra of the host galaxy of FRB 20220610A, covering the region of the [O II] lines with rest wavelengths 3726 and 3729 Å. The peak of the [O II] 3729 Å line in clump C is marked as a vertical dashed line for references. The red dashed line shows the uncertainty in the spectrum. The blue horizontal line shows zero relative flux.

S2 Supplementary Text

S2.1 Nature of the host galaxy

The spectra in Figure S3 indicate that components A and C are consistent in redshift to 0.01%, while component B is blueshifted by an amount equivalent to a velocity difference of just 150 km s^{-1} . With a projected separation of 16 kpc between compact components A and C, it is conceivable that they represent the two distinct nuclei of a merging or interacting system, while B is the gaseous tail linking them and currently drawn out towards the observer.

The measured $(R - K_s)$ colors for the individual clumps, as well as for the host system as a whole (1.70 ± 0.18) are unusually blue compared to those for field galaxies at redshifts around 1 (53–55). At $z = 1$ the $(R - K_s)$ color approximates rest-frame $(U - J)$. Starburst models, e.g. (56) only produce $(U - J)$ colors close to these values around 10 Myr after the onset of the burst, or at least 600 Myr later.

To model the stellar population of the host in more detail, we use the stellar population synthesis code `Prospector` (57) which performs Bayesian inference to determine the most likely stellar population based on the data and prior assumptions. We have used the integrated photometry from the entire complex to make an estimate of the host properties as there is insufficient information to characterize individual components. This effectively assumes that all components have the same star formation history. We fit the photometry using the stellar population synthesis library `python-fsps` (58, 59) and used the dynamic nested sampling routine `dynesty` (60) to sample the posteriors. Additional prior assumptions include a Chabrier IMF (61), Milky Way dust attenuation law (62), mass-metallicity relationship (63), a ratio on dust attenuation between old and young stars, and a *continuity* model non-parametric star formation history (SFH, (64)) using 8 age bins.

The photometry is best described by a galaxy of 1.2×10^{10} solar masses with an age of 1.02

Gyr. Additional parameters are reported in Table 1. The posterior probability show bimodality in age, mass, dust, and metallicity. This could be attributed to the known degeneracy in spectral energy distribution modeling for these parameters. However, given the complex morphology of the host, another interpretation of the bimodality is the presence of multiple stellar populations corresponding to multiple galaxies. Further imaging of the host with space-based facilities is required to disentangle the complex morphology in order to better characterize the host stellar population.

S2.2 Dispersion-measure analysis

Our DM analysis is based on the four-component model of (3),

$$DM_{\text{FRB 20220610A}} = DM_{\text{MW}} + DM_{\text{halo}} + DM_{\text{cosmic}} + \frac{DM_{\text{host}}}{1+z}, \quad (\text{S1})$$

where DM_{MW} is the Milky-Way disk DM contribution, DM_{halo} is the Milky Way halo contribution, DM_{cosmic} is the cosmic DM contribution and DM_{host} is the host DM contribution.

We assume the contribution from the Milky-Way interstellar medium (ISM) to be $DM_{\text{MW}}=31\text{pc cm}^{-3}$ from (30), and the halo contribution to be $DM_{\text{halo}}=50\text{pc cm}^{-3}$, which is on the low side of predictions from (23), but consistent with the observation of nearby, low-DM FRBs (65). The contribution from the intergalactic medium (IGM), including filaments and intervening halos, is a probabilistic distribution about the mean density of ionized gas in the universe (66). The full model is developed in (3), and implemented in the ‘FRB’ PYTHON library (67). We use cosmology from PLANCK (68), in particular $H_0 = 67.4\text{ km s}^{-1}\text{ Mpc}^{-1}$, and $\Omega_b h^2 = 0.0224$, and assume a ‘feedback’ parameter $F = 0.32$, which governs the clumpiness of cosmic gas distributions, and hence the variance of DM_{cosmic} about its expectation value. The remaining contribution is attributed to DM_{host} , which includes the FRB host galaxy halo and ISM, and any plasma in the immediate vicinity of the progenitor. This contribution is suppressed by a factor of $1+z$ (here, ~ 2), since the dispersion is induced at higher frequencies than those observed.

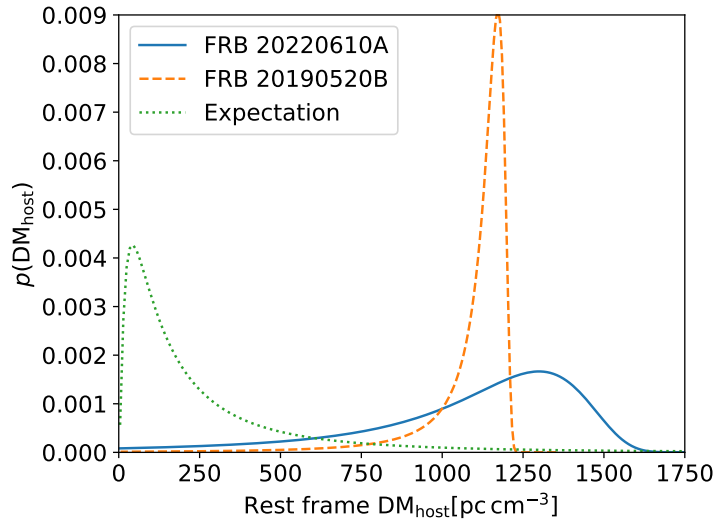


Figure S4: Probability distributions for the rest-frame host galaxy dispersion measures of FRB 20220610A (blue solid line) and FRB 20190520B (orange dashed line). The green dotted line shows the best-fit log-normal distribution for DM_{host} derived by the population modelling of (4).

Using Eq. (S1), we estimate the probability distribution of DM_{host} for FRB 20220610A in Figure S4. Since DM_{cosmic} is upwardly skewed, with the most likely DM being below the cosmic mean, and a small probability of very large excess DMs due to intersections with cosmic structures, our estimate for DM_{host} is left-skewed. The most likely value is $DM_{\text{host}} = 1304 \text{ pc cm}^{-3}$, with a 68% confidence interval of $(981, 1475) \text{ pc cm}^{-3}$. However, we cannot exclude the possibility of a negligible host contribution. We note that observational biases against high DM are irrelevant for this calculation, since we here only consider the relative contribution to DM from different sources, while the observational bias is fixed at the total observed value.

We also calculate the equivalent distribution for FRB 20190520B. This FRB, detected by the Five Hundred metre aperture Synthesis Telescope (FAST), originates from $z = 0.241$ (6). Its observed $DM_{20190520B} = 1204.7 \text{ pc cm}^{-3}$ implies a host galaxy contribution in the observer frame of 903_{-111}^{+72} . Using our model for DM_{cosmic} , DM_{halo} , and the value $DM_{\text{MW}} =$

60 pc cm⁻³ from (6), we find a rest-frame DM of 1172 pc cm⁻³ with a 68% confidence limit of (1104, 1197) pc cm⁻³. The predicted range is smaller due to the lower redshift of FRB 20190520B, and hence lower absolute variance in DM_{cosmic}.

Both values are much larger than the median DM_{host} of 186 pc cm⁻³ derived from population models (4). The lognormal distribution of DM_{host} is also shown in Figure S4 — while very high values of DM_{host} are disfavoured, they are allowed within the model.

It is likely therefore, but not certain, that FRB 20220610A has the highest intrinsic host galaxy DM of any known FRB.

S2.3 Burst energetics

FRB 20220610A was measured with a peak signal-to-noise (S/N) of 29.8 (which by definition has an uncertainty of ± 1) in CRAFT incoherent sum (ICS) data formed from 22 ASKAP antennas. The sensitivity in this configuration scales with $\sqrt{N_{\text{ant}}}$ compared to single-antenna searches (8), which have noise level of $N_{1\text{ms}} = 2.68 \pm 0.02$ Jy ms for a 1 ms burst (7, 69). Tests on pulsars comparing ICS to single-antenna mode have confirmed this scaling to within $97.5 \pm 2.5\%$.

The effective width of a burst in ICS data is increased from its intrinsic (after scatter-broadening) width by DM smearing over the 1 MHz channel bandwidth and by the time resolution of 1.182 ms. Thus S/N was maximized when the burst was integrated over four time samples. This corresponds to an initial band-averaged fluence estimate of $S/N N_{\text{ant}}^{-0.5} (\Delta t)^{0.5} N_{1\text{ms}} = 37$ Jy ms. This is a strict lower limit on the fluence, some of which will lie outside the 4-sample search window used by our real-time detection pipeline. Offline fitting of a Gaussian profile to the data produced a full-width half-maximum of 5.6 ms and integrated fluence of 43 ± 5 Jy ms. Including the potential inefficiency of ICS observations, and correcting for the offset from beam centre ($B = 0.98$ at central frequency), we estimate a band-averaged fluence

of $F_\nu = 45 \pm 5$ Jy ms.

The isotropic-equivalent spectral energy of transients is related to the observed fluence via

$$E_\nu = \frac{4\pi D_L^2}{(1+z)^2} F_\nu. \quad (\text{S2})$$

The FRB host galaxy has a redshift of 1.016 ± 0.002 , corresponding to a luminosity distance $D_L = 6929 \pm 2$ Mpc using Planck cosmology (68). We therefore find a spectral energy of $E_{\nu=2.543 \text{ GHz}} = 6.4 \pm 0.7 \times 10^{32} \text{ erg Hz}^{-1}$ at the mean emission frequency of 2.543 GHz.

The spectral behaviour of FRBs is complex, with some bursts showing broadband structure, and others being isolated in frequency (70). On average, bursts appear to be either brighter (71) or more common (4, 29) at lower frequencies. In the former case, fluence scales as $F_\nu \propto \nu^\alpha$, with a best-fit $\alpha = -1.5^{+0.2}_{-0.3}$ (71). If this is the correct behaviour, then a k-correction of $(1+z)^{-\alpha} = 2.85$ should be used to obtain $E_{\nu=1271.5 \text{ MHz}} = (1.8 \pm 0.2) \times 10^{33} \text{ erg Hz}^{-1}$; if not, $E_{\nu=1271.5 \text{ MHz}} = E_{\nu=2.543 \text{ GHz}}$.

S2.4 Implications for maximum FRB energy

Accurately modelling the maximum energy of FRBs, E_{max} , requires either a sample of localized bursts, or accounting for variations in the DM– z (‘Macquart’) relation. Furthermore, several parameters — such as source evolution, spectral behaviour, and the slope of the luminosity function — are correlated with E_{max} , and must be simultaneously fit to the data. This approach has been taken by several authors (28, 29, 72), who yield mutually consistent results. The most precise measurement — using a sample of 16 FRBs with measured redshifts, and 60 without — is $\log_{10} E_{\text{max}} [\text{erg}] = 41.26^{+0.27}_{-0.22}$ at 68% confidence (4). This calculation assumes an intrinsic emission bandwidth of 1 GHz, and does not include a k-correction, i.e., it allows for the rate of FRBs to vary with frequency, but not their energy. The burst energy function used is an upper incomplete gamma (Schechter) function, with differential slope $\gamma - 1$, and exponential cut-off of the form $\exp -E/E_{\text{max}}$. In this formalism, the burst energy of FRB 20220610A becomes

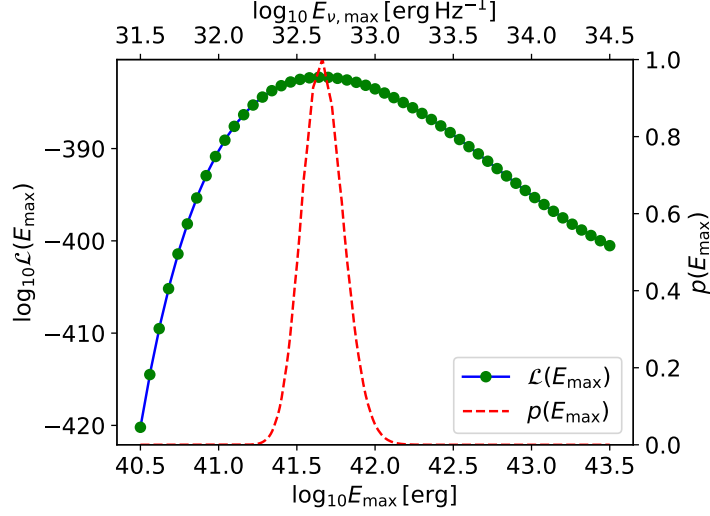


Figure S5: Estimation of the characteristic maximum FRB energy, E_{\max} . Shown are likelihoods \mathcal{L} evaluated when adding FRB 20220610A to the sample used by (4) and varying E_{\max} only, and the posterior probability distribution $p(E_{\max})$ assuming a log-uniform prior on E_{\max} .

$6.4 \pm 0.7 10^{41}$ erg, 3.5 times the cutoff energy — allowable, but unlikely, under this best-fit model.

To test the influence of this observation on E_{\max} , we use the model of (4) as implemented in (67, 73), add FRB 20220610A to the sample, and vary E_{\max} only. The obtained likelihoods are shown in Figure S5. The peak likelihood is obtained for $\log_{10} E_{\max} [\text{erg}] = 41.7 \pm 0.2$, i.e. $\log_{10} E_{\nu} [\text{erg Hz}^{-1}] = 32.7 \pm 0.2$, with error margins set by assuming a log-uniform prior on E_{\max} to produce a Bayesian posterior $p(E_{\max})$. This is 2.7 times greater than the previous best estimate, but still within the 90% confidence interval for $\log_{10} E_{\max} [\text{erg}]$ found by (4).

Nonetheless, FRB 20220610A is an unusually high-energy FRB. Given the time/frequency resolutions of the FRB detection algorithm ($t_{\text{samp}} = 1.182$ ms and $\Delta\nu = 1$ MHz respectively), the DM of 1457.624 ± 0.001 pc cm $^{-3}$ smears the signal over $w_{\text{DM}} = 5.8$ ms at band centre. Including the scattering time τ and intrinsic width w , the total effective width w_{eff} becomes

$$w_{\text{eff}} \approx \sqrt{w_{\text{DM}}^2 + t_{\text{samp}}^2 + w^2 + \tau^2} = 5.9 \text{ ms.} \quad (\text{S3})$$

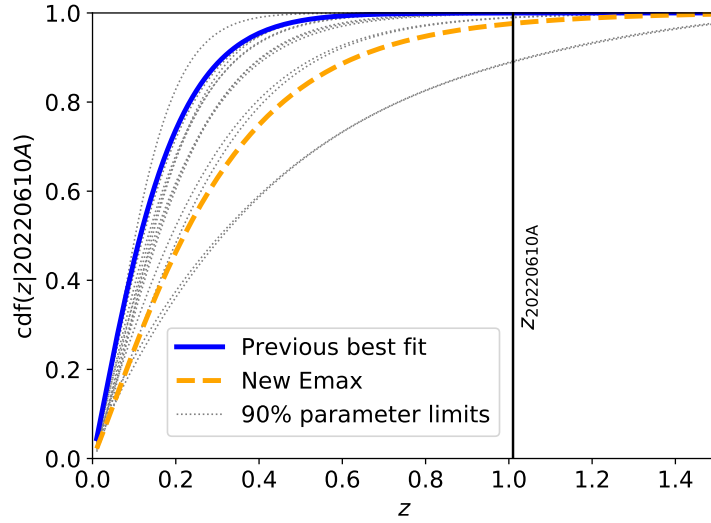


Figure S6: Cumulative probability $p(z|FRB\ 20220610A)$ for the redshift z of FRB 20220610A given its properties, estimated with the previous best-fit FRB population parameters of (4); population parameters varied within their 90% confidence limits; and with our new estimates of E_{\max} .

Without the w_{DM} , the width would be 1.35 ms. Since observed signal-to-noise scales with $w_{\text{eff}}^{-0.5}$, the greater width caused by the high DM of the burst has decreased sensitivity by 52%.

Using the observed properties of FRB 20220610A (DM, width, fluence), the observation parameters at time of detection (location in beam, observation frequency, sampling time, number of antennas), and estimates of the FRB population parameters, allows us to estimate the probability of observing FRB 20220610A at a given redshift, $p(z|FRB\ 20220610A)$. This is plotted in Figure S6. We use the previous best-fit population parameters (maximum energy E_{\max} , cumulative luminosity index γ , spectral rate scaling index α , scaling with the star-formation rate n_{sfr} , and log-mean and standard deviation of the host galaxy DM μ_{host} and σ_{host}) for $H_0=67.4\text{ km s}^{-1}\text{ Mpc}^{-1}$ from (4), and also set E_{\max} to our new best-fit value. We also explore parameter sets corresponding to these same parameters when at their upper and lower 90% confidence limits. The resulting cumulative probability distributions $\text{cdf}(z|FRB\ 20220610A)$ are

plotted in Figure S6.

S2.5 Limits on depolarization due to multi-path propagation

The depolarization f due to a spatially variable rotation measure in a foreground scattering screen can be modelled to be (14, 74)

$$f = 1 - \exp(-2\lambda^4\sigma_{\text{RM}}^2), \quad (\text{S4})$$

where f is the observed polarization fraction, λ is the observing wavelength and σ_{RM} parameterizes the RM complexity.

We can thus use our lower limit on polarization to set an upper limit on σ_{RM} using the relationship

$$\sigma_{\text{RM}} < \sqrt{-\frac{\log(1-f)}{2\lambda^4}} = 0.57 \text{ rad m}^{-2}. \quad (\text{S5})$$

assuming $f > 0.96$. In the frame of the host galaxy this corresponds to $\sigma_{\text{RM}} < 1.2 \text{ rad m}^{-2}$.

S2.6 The origin of the excess dispersion for FRB 20220610A

When considering possible origins for the excess dispersion seen for FRB 20220610A, we can make use of the additional information encoded by the burst’s propagation on the observed temporal scattering and rotation measure. In the rest frame of the host galaxy the pulse broadening is 1.88 ms, and the rotation measure is $860 \pm 8 \text{ rad m}^{-2}$. As the burst was detected at high Galactic latitude, the Milky-Way contribution to both scattering and rotation measure is small and can be neglected.

We first consider the possibility that the excess is associated with plasma closely associated with the burst source (a “circumburst” medium). Such an environment has been considered for some repeating FRB sources (6, 25). The excess dispersion seen in FRB 20220610A and the active repeating FRB source 20190520B are similar, but the pulse broadening is a factor

of 6 higher for FRB 20190520B, while the rotation measure of FRB 20190520B is highly variable but reaches values over an order of magnitude above that of FRB 20220610A (75). The frequency-dependent polarization seen in FRB 20190520B is consistent with multi-path propagation through a highly magnetized and turbulent local medium that could explain both the scattering and rotation measure; in this model, the rest-frame Faraday dispersion for this source is $\sigma_{\text{RM}} = 337 \text{ rad m}^{-2}$, over two orders of magnitude higher than the limit we derive for FRB 20220610A above. Thus, for the local environment to contribute the bulk of the excess DM seen in FRB 20220610A, the medium would need to be less turbulent and less highly magnetized than for FRB 20190520B.

Another possibility is that this excess arises in the interstellar medium (ISM) of the host galaxy. For that, it is useful to compare the properties of FRB 20220610A in the host galaxy rest frame to that of FRB 20190520B and pulsars in the Galaxy. In Figure S7, we show the distribution of DM and pulse broadening times for pulsars (30, 76) and localized FRBs. In the case of the FRBs we show the expected host DM contribution. FRB 20220610A shows significantly lower scattering than expected from Milky Way-like ISM. In Figure S8, we show the distribution of DM and rotation measures for pulsars (77) and the two FRBs. FRB 20220610A shows a rotation measure comparable to most Milky Way pulsars at similar DM, but much lower than the RM associated with pulsars close the Galactic Centre (78), some of which have DMs comparable to the upper end of the allowable range for FRB 20220610A.

So, while the Faraday rotation of the burst is not inconsistent with the relationship between dispersion and rotation measure observed in Galactic pulsars, for a Milky Way-like sightline, the observed excess DM would imply scatter broadening of $> 100 \text{ ms}$ at 1.4 GHz (11). Accordingly, we disfavour the host galaxy ISM as the sole source of the excess DM for FRB 20220610A.

A final possibility is that the excess DM is associated with plasma in an intervening structure along the line of sight but outside of the host galaxy complex. Identification would require

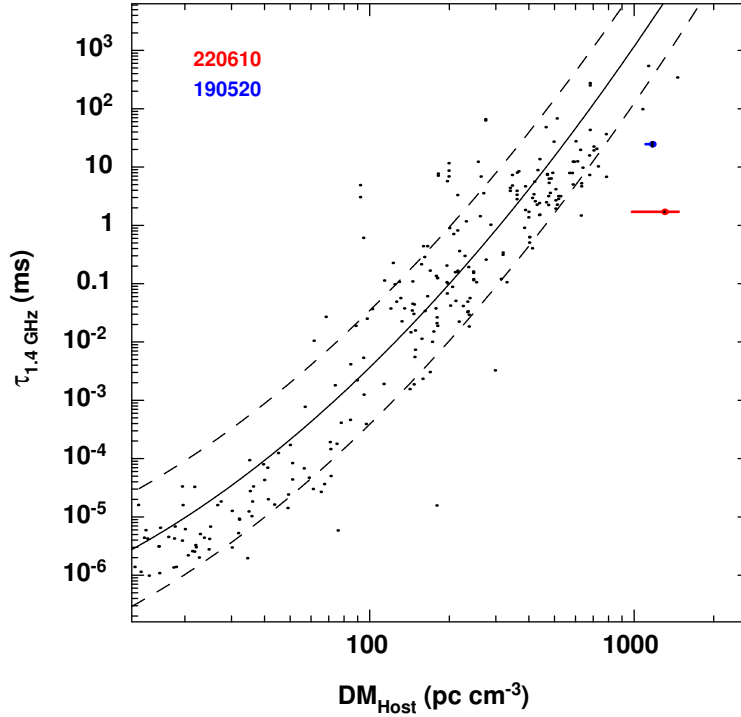


Figure S7: FRB and pulsar dispersion measure and scatter broadening times. We have increased the pulse broadening times of the FRBs by a factor of two to correct for their plane-wave scattering geometry.

detailed analysis of galaxies close to the burst line of sight (79). However, plasma in the intergalactic medium is not expected to harbour high levels of turbulence or magnetisation, so is not expected to cause the observed rotation measure or pulse broadening, and so this is (like the host galaxy ISM) disfavoured as the sole source of excess DM for FRB 20220610A (unless an intervening galaxy halo, where density and turbulence can be higher, contributed significantly).

Given the analysis above, it is not presently possible to definitively identify a dominant location for the excess DM seen in FRB 20220610A, but the observed properties can be plausibly reproduced by a combination of two (or, indeed, all three) of the potential locations.

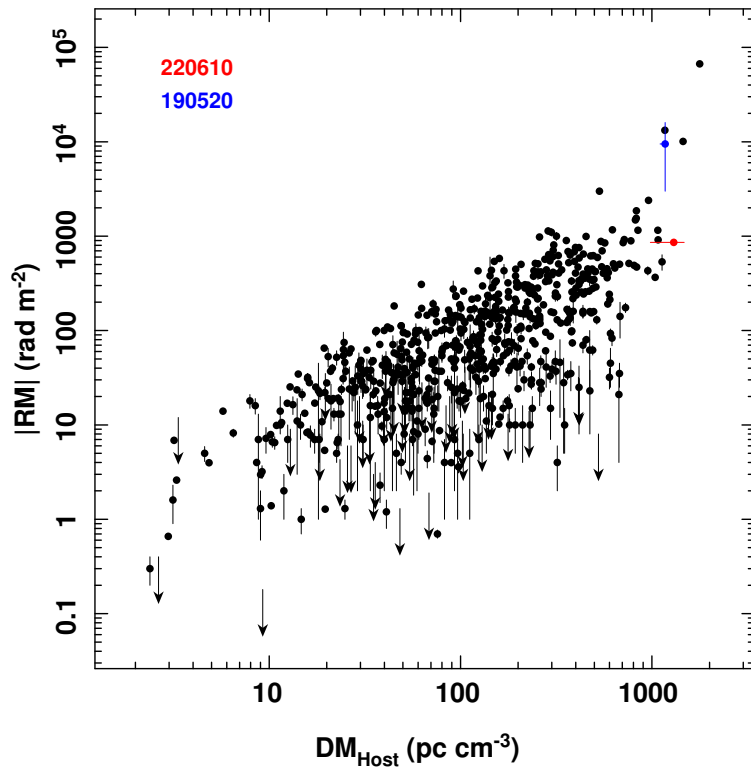


Figure S8: FRB and pulsar dispersion measures and rotation measures.